Power Electronic Systems
Laboratory

Proceedings of the 29th Applied Power Electronics Conference and Exposition (APEC 2014), Texas, Houston, USA, March 16-20, 2014

Accurate Finite-Element Modeling and Experimental Verification of Inductive Power Transfer Coil Design

R. Bosshard,
J. W. Kolar,
B. Wunsch

Eidgenössische Technische Hochschule Zürich
Swiss Federal Institute of Technology Zurich

Accurate Finite-Element Modeling and Experimental Verification of Inductive Power Transfer Coil Design

R. Bosshard*, J. W. Kolar*, and B. Wunsch†
*Power Electronic Systems Laboratory, ETH Zürich, Switzerland, Email: bosshard@lem.ee.ethz.ch
†ABB Switzerland Ltd., Corporate Research, 5405 Baden-Dättwil, Switzerland

***Abstract*—Inductive Power Transfer (IPT) is a promising technology for the charging of the traction batteries of electric and hybrid electric vehicles due to the significant simplification of the charging process implied by the contactless transmission of the charging energy. Typically, Finite-Element (FE) methods are used to predict the power loss in the IPT coils, to calculate equivalent circuit parameters, and to estimate the magnetic stray field of IPT coils. This paper gives insight into the FE modeling of the IPT coils of a 5 kW prototype IPT system with a dc-to-dc efficiency of more than 96% (52 mm air gap, coil diameter 210 mm). In the paper, modeling of IPT coils in the frequency domain using the FE tools FEMM and Ansys Maxwell is discussed and the calculation methods to predict power loss, equivalent circuit values, and stray fields are presented. The main part of the paper is a comprehensive experimental verification of the obtained FE results, which includes dc-to-dc conversion power loss, circuit parameter measurements, and measurements of the stray field. For the verification of the calculated stray fields the design of a highly compact, high-bandwidth, low-cost magnetic field probe is presented. Experimental data obtained from the designed field probe shows that the FE tools used in the design of the IPT coils deliver field data with a calculation error of less than 5%.**

I. Introduction

Inductive Power Transfer (IPT) is widely discussed as a charging technology for the traction batteries of Electric and Hybrid Electric Vehicles (EV/HEV) [1]–[5]. In this application, IPT offers an advantage compared to traditional charging infrastructure as it significantly simplifies the charging process and, therefore, increases the usability and the convenience for the user. Hence, IPT could be a crucial factor for a further increase of the popularity of EV/HEV and a driver for a reduction of the global consumption of fossil fuels.

IPT systems designed for EV/HEV applications employ a transmitter coil, which is placed on or embedded into the road surface, to transmit the required charging energy via a magnetic flux to a receiver coil mounted to the underfloor of the EV/HEV, similar to a traditional transformer. Due to the inherently large air gap of typically 100-300 mm, the leakage flux of the transformer is high and resonant capacitors must be used to compensate the resulting leakage inductance. Depending on the geometrical design of the coils and the transmitted power, the limit values for the magnetic stray fields in regions accessible to humans as specified in the relevant standards become an important design aspect [6], [7]. At power levels of several kW shielding is often required in addition to the used magnetic core materials in order to reduce the stray flux density [2], [8].

Typically, Finite-Element (FE) methods are used to calculate the magnetic properties of an IPT inductor during the design process. The obtained results are used to predict circuit parameters, power loss, and the magnetic stray field before an actual prototype is built. This paper aims to give a detailed insight into the modeling of IPT coils with FE tools. The paper presents the models used for the design of a 5 kW-IPT prototype system (cf. **Fig. 1**) that achieves a dc-to-dc efficiency of more than 96% when transmitting across an air gap of 52 mm using transmission coils that measure 210 mm in diameter. The IPT coils shown in **Fig. 1(b)** were modeled and optimized with the aid of the FE tools FEMM and Ansys Maxwell. In the first part of the paper, the modeling of the IPT coils in the FE tools and the calculation of the power loss in the employed copper litz wire as well as in the core material shown in **Fig. 1(c)** is discussed. An additional focus is set to the reliable calculation of the stray field. The prototype system is presented in more detail in Section II. The used FE models and the calculations are presented and discussed in Section III.

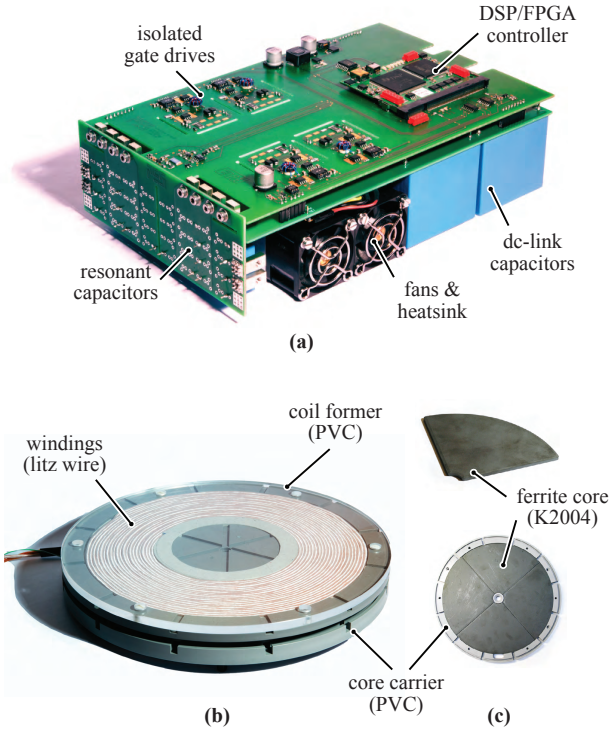

Fig. 1. **(a)** Prototype IPT system, designed to transmit 5 kW across an air gap of 52 mm at 100 kHz: test inverter employing SiC MOSFETs, **(b)** IPT coil with a diameter of 210 mm, windings made from copper litz wire with 630 strands of 71 µm diameter, and **(c)** ferrite core material (K2004) placed in a carrier made from PVC.

An FE-assisted design process relies heavily on the calculation accuracy of the used FE method. Consequently, an experimental verification of the FE methods is advisable to prevent design errors. For instance [9] presents a verification of the results for the power loss due to eddy currents and for the stray field obtained from a 3D-FE analysis of a dry-type transformer. Magnetic field measurements with a Hall effect sensor show that the calculation error of the used FE tool is 7% for the total power loss, 10% for the near stray field, and 20% for the far stray field. To the knowledge of the authors, a comparable verification regarding the aspects specific to IPT systems cannot be found in literature. Therefore, the main focus of this paper is a comprehensive experimental verification of the FE calculation

978-1-4799-2325-0/14/$31.00 ©2014 IEEE

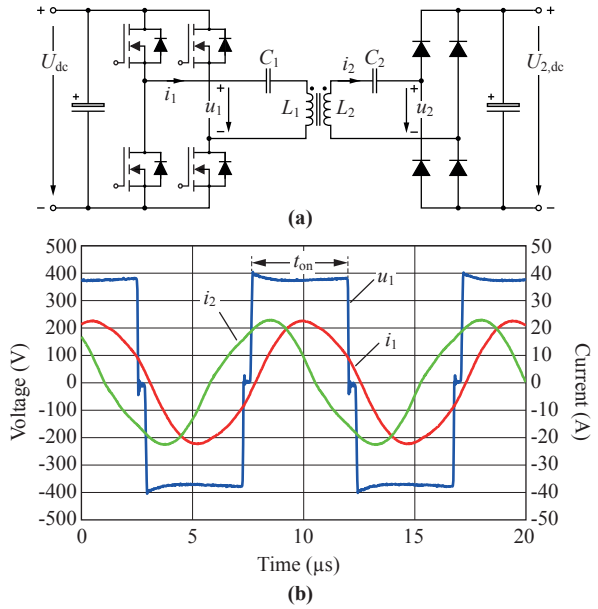

Fig. 2. **(a)** IPT system with a series-series compensation of the leakage inductance, a full-bridge inverter comprising SiC-MOSFETs (CMF20120D), and a diode rectifier (DSEI2x101); **(b)** waveforms of a measurement at the transmission of 5 kW over an air gap of 52 mm.

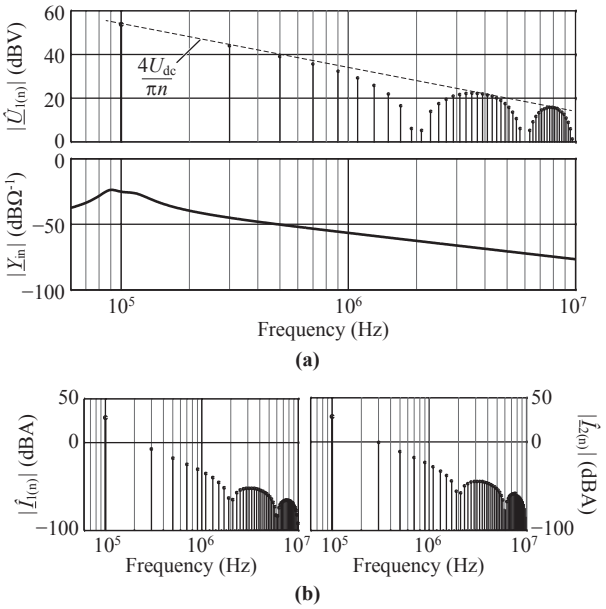

Fig. 3. **(a)** Spectrum $\underline{\hat{U}}_{1(n)}$ of the block-shaped voltage at the input of the resonant tank and magnitude of the input admittance $\underline{Y}_{in}$ as a function of the frequency (parasitic capacitances neglected); **(b)** spectra of the primary coil current $\underline{\hat{I}}_{1(n)}$ and the secondary coil current $\underline{\hat{I}}_{2(n)}$. It can be seen that the fundamental components of both currents are more than 30 dBA higher than the first non-zero harmonic component.

results obtained from the FE models for the 5 kW IPT prototype system.

A validation of the calculated circuit parameters and the losses in the magnetic components as well as in the components of the power converter is straight-forward. However, a verification of the calculated stray field usually requires dedicated measurement equipment. Therefore, in this paper it is shown how a highly compact, high-bandwidth, low-cost magnetic field probe with a high measurement accuracy can be built. Its design as well as the used field measurement setup is presented in Section IV. In order to asses the accuracy of the designed field probe, measurement results are compared to those obtained from the commercial field probe Narda ELT-400. The results of this comparison are given in the same section. In Section V, the predicted circuit parameters, power loss, and stray fields that were obtained from the FE methods are compared to measurements and the accuracy of the FE methods is discussed. Section VI concludes the paper and gives an outlook on future work.

II. 5 kW-Prototype IPT System

For an experimental verification of the results of previous research [10], [11], the prototype IPT system shown in **Fig. 1** was designed for the transmission of 5 kW of output power across an air gap of 52 mm. To compensate the high leakage inductance of the transmission coil shown in **Fig. 1(b)**, a series compensation of the secondary is used as shown in **Fig. 2(a)**. The value of the resonant capacitor C_2 was chosen according to the condition $\omega_0 L_2 = 1/(\omega_0 C_2)$, where L_2 is the self-inductance of the receiver coil and $\omega_0 = 2\pi f_0$ is the angular resonant frequency. This choice for the secondary-side resonant capacitance ensures that only active power is transmitted through the air gap. For an ohmic load that is matched to the receiver impedance $\omega_0 L_2$ according to the matching condition given in [11]–[13], this means that at the resonant frequency f_0 the smallest physically possible total power loss occurs in the IPT inductors.

In order to reduce the reactive power required to drive the resonant tank, another resonant capacitor C_1 is used at the primary side of the link. Its value is chosen such that the input impedance $\underline{Z}_{in}$ is purely ohmic at the resonant frequency f_0, i.e. $C_1 = 1/(\omega_0^2 L_1)$. The selection of the resonant frequency $f_0 = 100$ kHz resulted from a trade-off between the losses in the power converter and the required size of the inductor coils. Further insight into the design of the resonant system as well as the power converter is subject of an upcoming publication by the authors.

For the experiments shown in this paper, the resonant tank was driven from a 375 V dc-link using a full-bridge inverter that employs SiC-MOSFETs (Cree CMF20120D) as switches as shown in **Fig. 1(a)**. On the secondary side, a fast diode bridge (DSEI2x101) is used to produce a dc output voltage. Measured waveforms of the inverter output voltage u_1, the primary current i_1, and the secondary current i_2 during transmission of 5 kW are shown in **Fig. 2(b)**. The inverter at the primary side is operated at a switching frequency of $f_{sw} \approx 105$ kHz, which is slightly above the resonance frequency of the tank. This ensures Zero Voltage Switching (ZVS) of the MOSFETs in the inverter bridge legs. The bridge legs are operated with a phase shift of 170° to achieve a voltage transfer ratio of approximately 1:1. A self-oscillating controller is used to synchronize the inverter to the resonance frequency of the tank, which makes it highly tolerant to misalignment of the coils and to component tolerances. The dc-to-dc efficiency of the IPT system at the operating point shown in **Fig. 2(b)** is 96.5% at an air gap of 52 mm, including losses in the IPT coils, the resonant capacitors, and in the semiconductors. This will be discussed in more detail in Section V.

As the electromagnetic design with FE tools is typically performed in the frequency domain, a first step is to analyze the spectra of the voltage and current waveforms in order to determine which harmonic orders have to be taken into account. For the rectangular voltage waveform of the inverter bridge-legs, the spectrum is calculated as

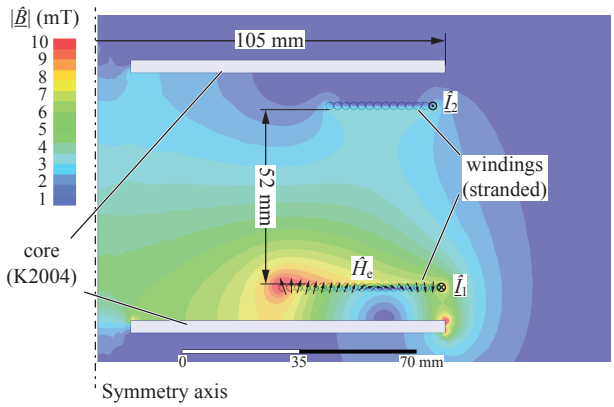

Fig. 4. Visualization of the magnetic flux density on the used FE model in Ansys Maxwell. Schematically drawn is the vector of the external magnetic field $\hat{H}_\mathrm{e}$ in the primary windings (not to scale).

$$|\hat{\underline{U}}_{1(\mathrm{n})}| = \frac{4}{\pi}\frac{U_\mathrm{dc}}{n}\sin\left(n f_\mathrm{sw} t_\mathrm{on}\pi\right) \tag{1}$$

for odd harmonic orders n and the duration t_on of the power interval defined as indicated in **Fig. 2(b)**. The spectrum of the voltage waveform u_1 is given in **Fig. 3(a)**. The resulting currents in the IPT coils i_1 and i_2 both depend on the magnitude of the input admittance $\underline{Y}_\mathrm{in} = \underline{Z}_\mathrm{in}^{-1}$, which is also shown in **Fig. 3(a)**. From the spectra of the inductor currents, which are given in **Fig. 3(b)**, it is evident that their fundamental component is more than 30 dBA larger than their first non-zero harmonic component. Accordingly, it is sufficient to use the fundamental frequency of the system for the FE models and neglect all higher harmonic orders.

In the following, the FE models used for the design of the transmission coils of the IPT prototype system at hand are presented and the methods for the loss calculations are outlined. Later on, the results obtained from these models will be experimentally verified.

III. FE-Modeling of IPT Coils

For coil designs that include core materials or have unconventional geometric shapes, FE tools are required for the optimization as analytical calculations are hardly possible. These tools allow calculating equivalent circuit parameters of the coil, predicting the electromagnetic losses in the used materials, dimensioning of the core to avoid saturation, as well as calculation of the stray fields.

For the prototype presented in the previous section, the FE tools FEMM[1] and Ansys Maxwell[2] were used for this purpose. The used frequency domain FE models and their implementation including boundary conditions and meshing are discussed below. In the last part of this section, the calculations for the loss estimation are given.

A. Axis-Symmetric FE-Models

The coil design that was chosen for the IPT prototype presented in the previous section is axis-symmetric. Hence, two dimensional FE models are sufficient for the calculation. **Fig. 4** shows the simulation model used in the FE tools FEMM and Ansys Maxwell. The litz wire winding is modeled as cylinders of stranded wire with a uniform current density as in the dc case. This prevents the time-intensive calculation of eddy currents in the windings. This approximation is valid because 1) the litz wire strand diameter was chosen to reduce the high-frequency effects to a minimum, 2) the current distribution inside the windings has only little influence on the magnetic field on the outside for the investigated geometry, and 3) because in the following the losses in the windings are calculated using analytical equations together with field values obtained from the FE results and not with the tools provided by the FE method itself. Both of the used FE tools offer this functionality to accelerate their ac-calculation modules.

The core is modeled by the relative permeability of the material (K2004 in the prototype: μ_r = 2000). The conductivity of the core material is low, therefore, it is neglected in the FE model ($\sigma <$ 1 S/m). All magnetically inactive materials are not modeled, because capacitive effects were excluded from the calculations, which is valid at the considered frequency.

In both tools, the simulated space is bounded by a sphere with a radius that is several times larger than the coil radius. The sphere radius was determined from a sequence of simulations where the size of the bounding sphere was increased stepwise until no further change in the simulation results could be observed. This process resulted in a sphere radius four times larger than the coil radius. A mixed Dirichlet/Neumann boundary condition on the border of the sphere is chosen to model unbounded, open space. In Ansys Maxwell, the appropriate boundary condition is called *Balloon*. In FEMM, the same can be achieved by setting up an appropriate mixed boundary condition manually[3].

Automatic meshing was used in both cases, which leads to a skin depth based mesh in all materials. To increase the accuracy of the stray field calculation, a maximum mesh size of 5 mm was specified along a radial axis, which has its origin in the center of the air gap. The stray field is then evaluated along this axis.

B. Power Loss Calculation

Because the calculation of the power loss in litz wire is not supported by some FE tools (e.g. Ansys Maxwell), a combination of analytical and FE-assisted calculations is preferred for the loss estimation. The conduction loss in the copper litz wire windings due to the skin effect (including dc conduction loss) can be calculated analytically by integrating

$$p_\mathrm{skin} = n \cdot R_\mathrm{dc} \cdot F_R(f_0) \cdot \left(\frac{\hat{I}}{n}\right)^2 \tag{2}$$

over the total length of the windings. The variable n denotes the number of isolated strands in the litz wire, R_dc is the dc resistance per unit length of a single strand of the litz wire, $\hat{I}$ is the current peak value, and $F_R(f_0)$ is a frequency dependent factor that models the skin effect [14].

The calculation of the copper loss due to the proximity effect

$$p_\mathrm{prox} = n \cdot R_\mathrm{dc} \cdot G_R(f_0) \cdot \left(\hat{H}_\mathrm{e}^2 + \frac{\hat{I}^2}{2\pi^2 d_\mathrm{a}^2}\right), \tag{3}$$

where d_a is the outer diameter of the litz wire and $G_R(f_0)$ denotes a frequency dependent factor that models the proximity effect [14], however, requires knowledge of the external magnetic field $\hat{H}_\mathrm{e}$ penetrating the windings. It is a good assumption that the magnetic field is equal over the total length of one turn of the axis-symmetric inductor model. However, the external magnetic field $\hat{H}_\mathrm{e}$ differs from turn to turn (cf. **Fig. 4**). Therefore, $\hat{H}_\mathrm{e}$ must be evaluated in the center of each turn individually to calculate the loss density p_prox accurately

[1] Version 4.2, freeware available at www.femm.info (25.10.2013).
[2] Version 16.0, available at www.ansys.com (25.10.2013).
[3] See www.femm.info/Archives/doc/tutorial-magnetic.pdf (25.10.2013).

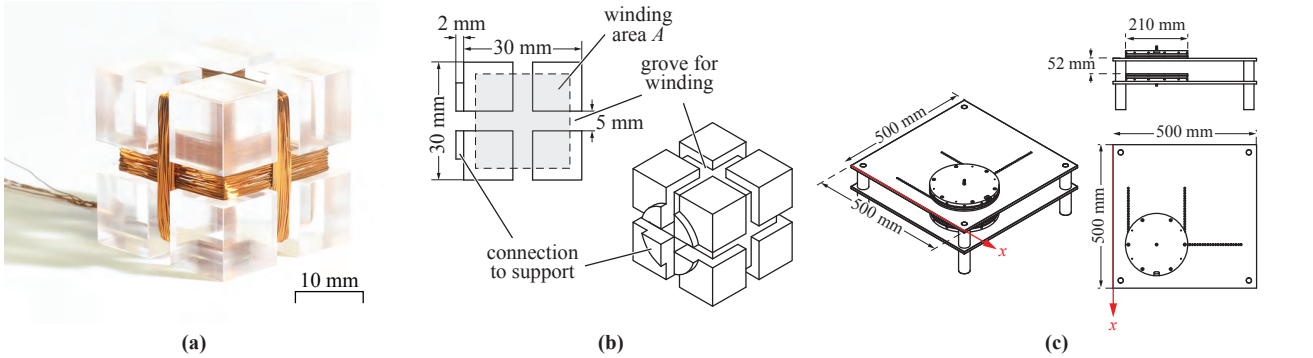

Fig. 5. **(a)** Photograph and **(b)** construction drawing of the field probe designed for the verification of the FE-calculated stray field of the IPT prototype system. A machined PMMA cube is used to support three windings (one for each spatial component of the field vector) of 40 turns each. An amplification circuit and an oscilloscope are used to measure the induced voltage in each winding. **(c)** Measurement setup including the IPT coils: indicated in red is the x-axis used for the reference measurements shown in **Fig. 7**.

for each turn. The loss density p_{prox} is then multiplied with the length of the individual turn. In a three dimensional design, an integration along each turn would be required. The total power loss due to the proximity effect can then be calculated by adding up the power losses of all turns in a coil.

The core loss can be calculated by integrating the core loss density according to the Steinmetz equation

$$p_{\mathrm{core}} = \kappa \cdot f_0^{\alpha} \cdot \hat{B}^{\beta} \tag{4}$$

over the volumes of the two cores. The parameters κ, α, and β are the Steinmetz parameters of the core material (K2004 in the prototype: κ = 6.47, α = 1.32, β = 2). In Ansys Maxwell, this calculation is straight-forward with the field calculator. With FEMM, it has to be implemented manually using one of the scripting interfaces.

Using the FE models and calculation methods presented in this section, the circuit parameters and the power loss of the IPT coils can be estimated. An experimental verification of these prediction is shown in the last part of the paper. For a verification of the predicted stray field, an appropriate sensor is needed. Therefore, the design and implementation of a high-bandwidth, low-cost magnetic field probe is the subject of the next section.

IV. Design of a High-Bandwidth Field Probe

Several sensor technologies exist for measurements of magnetic fields, which differ largely in terms of sensitivity, bandwidth, and cost [15]. Even though Hall effect sensors would offer a cost advantage and would allow for a highly integrated design of the probe, their sensitivity and bandwidth is typically lower than induced voltage sensors. Therefore, for the design frequency of 100 kHz, a field probe based on measurements of induced voltage was implemented. For the measurement of the induced voltage caused by the three spatial components of the magnetic flux density vector, three sensor windings were arranged perpendicularly on a cubic supporter made from plexiglass (PMMA), which is shown in **Fig. 5(a)-(b)**.

The geometrical size and the number of turns N of the probe were chosen such that induced voltages of around 10-15 mV/µT are reached at a frequency of 100 kHz, which is suitable for state-of-the-art measurement electronics. To limit the parasitic capacitance of the winding in order to reach a high bandwidth, a low number of turns is desirable. Hence, a larger area must be enclosed by the windings to reach a sufficient signal amplitude. However, because a compact design is preferred for precise point-measurements of the magnetic

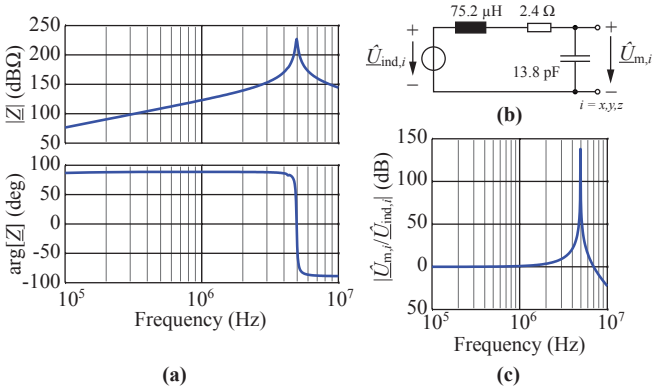

Fig. 6. **(a)** Measured frequency response of the winding; **(b)** derived equivalent circuit; **(c)** resulting transfer function from the induced voltage in the windings $\underline{\hat{U}}_{\mathrm{ind}}$ to the measured voltage $\underline{\hat{U}}_{\mathrm{m}}$ at the probe terminals.

flux density, the side length of the PMMA supporter was chosen as 30 mm considering the trade-off. The windings are placed in 5 mm wide groves that were cut into the faces of the supporter, resulting in a winding area of A = 576 mm^2 as indicated in **Fig. 5(b)**.

Under the assumption of an approximately constant flux density on the whole winding area A, the voltage induced in the winding with spatial orientation $i \in [x, y, z]$ can be calculated from Faraday's law

$$u_{\mathrm{ind},i}(t) = \frac{\mathrm{d}}{\mathrm{d}t} \iint_{A_i} \vec{B}(t) \mathrm{d}\vec{A}_i \approx NA \cdot \frac{\mathrm{d}}{\mathrm{d}t} B_i(t), \tag{5}$$

where $\vec{B}(t) = [B_x(t), B_y(t), B_z(t)]^{\mathrm{T}}$ denotes the magnetic flux density vector crossing the winding area A. In the frequency domain, it can be seen from

$$|\underline{\hat{U}}_{\mathrm{ind},i}| = \omega NA \cdot |\underline{\hat{B}}_i|, \tag{6}$$

that N = 40 will lead to $\underline{\hat{U}}_{\mathrm{ind},i}/\underline{\hat{B}}_i$ = 14.5 mV/µT at the fundamental frequency of 100 kHz. From the measurement of the induced voltage, the corresponding values of the magnetic flux density can be determined using

$$|\underline{\hat{B}}| = \frac{1}{\omega NA} \sqrt{\sum_{i \in [x,y,z]} |\underline{\hat{U}}_{\mathrm{ind},i}|^2}. \tag{7}$$

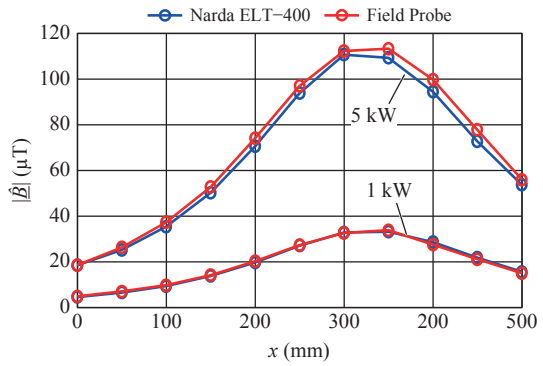

Fig. 7. Comparison of field measurements along the x-axis marked in **Fig. 5(c)**, taken once with the commercial device Narda ELT-400 and once the field probe presented in the paper.

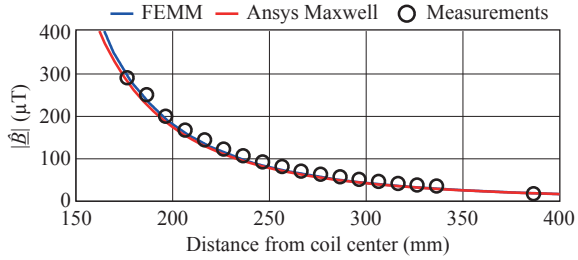

Fig. 8. Comparison of calculated and measured stray field of the IPT system. The average of the absolute value of the relative error with respect to the measurements is 9.3% for FEMM and 11.6% for Ansys Maxwell.

The sensor windings are made from copper wire with a diameter of 0.2 mm. The turns are arranged on two layers in order to obtain an approximately concentrated winding, which is desirable for a measurement of the magnetic flux density at a specific point. The evaluation of a second prototype with the same number of turns and the same copper cross section, but with only one layer of turns indicated that the reduced parasitic capacitance and consequently a higher measurement bandwidth is of limited benefit, due to the additional measurement error resulting from the geometrically less concentrated winding arrangement.

A measurement of the impedance of the designed probe winding is shown in **Fig. 6(a)**. From the measurement, the parameters of the equivalent circuit shown in **Fig. 6(b)** were derived. It can be seen from the frequency response in **Fig. 6(c)** that a measurement bandwidth of up to several MHz an be reached with the presented probe. In case measurements close to the self-resonant frequency of the winding are required, the magnitude of the transfer function $\underline{\hat{U}}_\mathrm{m}/\underline{\hat{U}}_\mathrm{ind}$ shown in **Fig. 6(c)** must be taken into account. This could be done by including a frequency dependent correction of the measured voltage according to this transfer function in (7). Alternatively, damping of the coil self-resonance could be provided.

For accurate measurements of the voltage at the winding terminals, a voltage-follower circuit with unity gain using an operational amplifier (OPA820) was implemented for each spatial dimension on a measurement PCB. The voltage-follower configuration is used for its high input impedance, which results in a high impedance measurement. This is needed because any loading of the sensor windings would lead to distortion of the results. The measurement electronics were placed at a distance of approximately 50 mm from the sensor windings to avoid possible field disturbances, e.g. due to the components, or a ground plane of the PCB.

TABLE I
COMPARISON OF FE MEASURED AND CALCULATED CIRCUIT PARAMETERS (AIR GAP 52 MM)

Variable	Measured	FEMM	Ansys Maxwell
L_1	122 µH	129.9 µH (+6.5%)	126.8 µH (+3.9%)
L_2	70.3 µH	72.4 µH (+3%)	71.4 µH (+1.6%)
L_h	30.6 µH	33.9 µH (+10.7%)	33.3 µH (+8.8%)
k	0.33	0.35 (+6.1%)	0.35 (+6.1%)

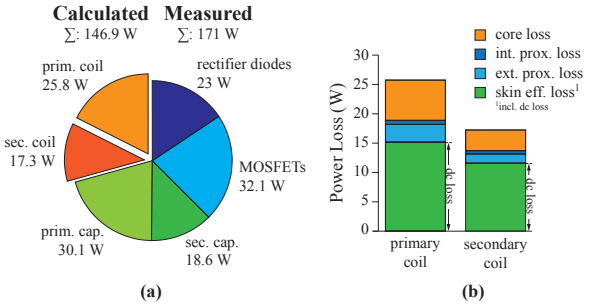

Fig. 9. **(a)** Calculated loss components contributing to the total dc-to-dc conversion losses of the prototype IPT system. The calculated total loss is 146.9 W, measured were 171 W (-14.2%); **(b)** FE-calculated loss components in the IPT coils.

In order to verify the functionality of the field probe, measurements of the magnetic flux density were performed on the measurement setup shown in **Fig. 5(c)**. Measurements were taken with the presented field probe along the indicated x-axis. Additionally, measurements with the commercial field probe Narda ELT-400 were taken at the same locations. A comparison of the obtained results from both probes is shown in **Fig. 7**. The deviation of the measurements obtained from the probe presented in this paper with respect to the commercial device is below 5% for all positions, even for flux density values as low as 5 µT.

V. VERFICATION OF THE FE MODELS

In order to assess the quality of the FE models presented in Section III in terms of calculated power loss, equivalent circuit parameters, and stray field, an extensive experimental verification was performed. In the following, the results of these measurements are compared to the calculated results.

A. Equivalent Circuit Parameters

Table I shows the measured circuit parameters and those obtained from the FE methods. Indicated in brackets is the calculation error relative to the measured values. It can be seen, that the self-inductances are calculated accurately by both of the used FE tools. The magnetic coupling is also accurate with an error of less than 10%. The highest error appears for the mutual inductance, because in its calculation according to $L_\mathrm{h} = k\sqrt{L_1 L_2}$ the calculation errors in the self-inductances and the magnetic coupling are added up.

B. Stray Field

To verify to accuracy of the stray field calculation, field measurements were taken with the field probe presented in Section IV along a radial axis, which has its origin in the center of the air gap. The measurements of the stray field are indicated in **Fig. 8**, together with the values calculated by the FE tools. When the relative error of the calculation is averaged in absolute value, the tool FEMM shows a deviation of 9.3%. Ansys Maxwell deviates by 11.5% from the measured field values.

C. Power Loss

Due to the high frequency of the coil currents and the steep slopes of the switched voltage, it is difficult to reliably measure the power loss in the resonant tank directly. For this reason, only measurements of the dc input power and the dc output power were taken. The measured power loss was then compared to the calculated values of the losses in all components of the prototype system, which are shown in **Fig. 9(a)**. The coil losses were calculated as outlined in Section III. For the calculation of the losses in the resonant capacitors, the loss tangents indicated by the manufacturer were used. Thanks to the ZVS operation of the MOSFETs and because an external auxilary supply is used to power the gate drivers, only conduction losses have to be included for the semiconductor losses of the primary side inverter. Also the rectifier diodes on the secondary are soft-switched and, therefore, only conduction losses have to be calculated also for the semiconductor losses of the receiver.

The comparison in **Fig. 9(a)** shows that the coil losses contribute only about 30% of the total loss, while the remaining loss occurs to approximately equal parts in the resonant capacitors and in the semiconductor devices. This clearly illustrates that for a holistic optimization of the IPT system, these components must be considered. This is the subject of current research.

The partitioning of the calculated coil losses into skin effect loss (including dc conduction loss), proximity effect loss, and core loss is given in **Fig. 9(b)**. It can be seen that thanks to the small strand diameter of the used litz wire (71 µm), the main parts are the dc conduction losses. Approximately 24% of the total power loss in the coils result from core losses.

The calculated total loss is 146.9 W, which means a calculation error of -14.2% with respect to the measured 171 W dc-to-dc power loss. The calculation accuracy of the losses in the resonant capacitors and the semiconductors can be considered high as the calculation is directly based on manufacturer data. All in all, this indicates a good agreement of the FE results with the measurements.

VI. Conclusion

This paper presents an experimental verification of the FE calculations used in the design of the transmission coils of a 5 kW IPT prototype system, which achieves an efficiency of more than 96% at an air gap of 52 mm (coil diameter 210 mm).

In the first part of the paper, the used FE models are presented and it is outlined how the power loss in the IPT inductor is calculated in a combined approach using FE results and analytical calculations. The calculated power loss was compared to the experimental data obtained from a dc-to-dc loss measurement. The power loss calculation shows a calculation error of -14.2% in the total power loss, which is considered a good agreement between calculation and measurement.

The calculated circuit parameters of the coils are also accurate with an error below 6.5% for self-inductances, below 6.1% for the magnetic coupling, and below 10.7% for the mutual inductance.

For the verification of the stray field that was calculated with the same FE method, a high-bandwidth, low-cost field probe was designed. A comparison to reference measurements obtained from a commercial probe Narda ELT-400 show a high accuracy of the field probe with a measurement error of 5% at flux densities as low as 5 µT. The presented field probe was used to verify the stray field calculated with the FE method. It is shown that the calculation error is 9.3% for the FE tool FEMM and 11.6% for Ansys Maxwell.

Future research will address the system-oriented multi-objective optimization of high-power IPT systems taking into account the losses in the magnetic components as well as those in the remaining parts of the power electronics. Upcoming publications will also provide comprehensive design guidelines and scaling laws for IPT systems that are generally valid and can be applied to any power level.

Acknowledgment

The authors would like to thank ABB Switzerland Ltd. for their funding and for their support regarding many aspects of this research project. Additionally, the authors would like to thank the students Michael Haider and Julien Thomas for their experimental work related to this publication.

References

[1] C.-S. Wang, O. H. Stielau, and G. A. Covic, "Design considerations for a contactless electric vehicle battery charger," *IEEE Trans. Ind. Electron.*, vol. 52, no. 5, pp. 1308–1314, 2005.

[2] J. Kim, J. Kim, S. Kong, H. Kim, I.-S. Suh, N. P. Suh, D.-H. Cho, J. Kim, and S. Ahn, "Coil design and shielding methods for a magnetic resonant wireless power transfer system," *Proc. IEEE*, vol. 101, no. 6, pp. 1332–1342, 2013.

[3] B. Goeldi, S. Reichert, and J. Tritschler, "Design and dimensioning of a highly efficient 22 kW bidirectional inductive charger for e-mobility," in *Proc. Int. Exhibition and Conf. for Power Electronics (PCIM Europe)*, 2013, pp. 1496–1503.

[4] D. Kürschner, F. Turki, C. Yotta, S. Thamm, and C. Rathge, "Comparison of planar and solenoid coil arrangements for inductive EV-charging application," in *Proc. Int. Exhibition and Conf. for Power Electronics (PCIM Europe)*, 2013, pp. 385–391.

[5] Z. Pantic, K. Lee, and S. Lukic, "Inductive power transfer by means of multiple frequencies in the magnetic link," in *Proc. 5th Energy Conversion Congr. and Expo. (ECCE USA)*, 2013, pp. 2912–2919.

[6] ICNIRP, *Guidelines for limiting exposure to time-varying electric, magnetic and electromagnetic fields (up to 300 GHz)*, Std., 1998.

[7] ——, *Guidelines for limiting exposure to time-varying electric and magnetic fields (1 Hz to 100 kHz)*, Std., 2010.

[8] M. Budhia, J. Boys, G. Covic, and C. Huang, "Development of a single-sided flux magnetic coupler for electric vehicle IPT charging systems," *IEEE Trans. Ind. Electron.*, vol. 60, no. 1, pp. 318–328, 2013.

[9] J. Smajic, T. Steinmetz, B. Cranganu-Cretu, A. Nogues, R. Murillo, and J. Tepper, "Analysis of near and far stray magnetic fields of dry-type transformers: 3-D simulations versus measurements," *IEEE Trans. Magn.*, vol. 47, no. 5, pp. 1374–1377, May 2011.

[10] R. Bosshard, J. Mühlethaler, J. W. Kolar, and I. Stevanovic, "Optimized magnetic design for inductive power transfer coils," in *Proc. 38th Applied Power Electronics Conf. and Expo. (APEC)*, 2013, pp. 1812–1819.

[11] ——, "The η-α-Pareto front of inductive power transfer coils," in *Proc. 38th Industrial Electronics Conf. (IECON)*, 2012, pp. 4270–4277.

[12] E. Waffenschmidt and T. Staring, "Limitation of inductive power transfer for consumer applications," in *Proc. 13th European Conf. on Power Electronics and Applications (EPE)*, 2009, pp. 1–10.

[13] K. V. Schuylenbergh, *Inductive powering: basic theory and application*, 1st ed. Springer Science, 2009.

[14] J. Mühlethaler, "Modeling and multi-objective optimization of inductive power components," Ph.D. dissertation, Swiss Federal Institute of Technology Zurich (ETHZ), 2012.

[15] J. Lenz and S. Edelstein, "Magnetic sensors and their applications," *IEEE Sensors J.*, vol. 6, no. 3, pp. 631–649, Jun. 2006.